IEEE Access
Multidisciplinary | Rapid Review | Open Access Journal

Received December 14, 2020, accepted December 29, 2020, date of publication January 11, 2021, date of current version January 22, 2021.

Digital Object Identifier 10.1109/ACCESS.2021.3050920

An Improved Technique for Energy-Efficient Starting and Operating Control of Single Phase Induction Motors

MUHAMMAD NOMAN ALMANI[1], GHULAM AMJAD HUSSAIN[2], (Senior Member, IEEE), AND ASHRAF A. ZAHER[2], (Senior Member, IEEE)

[1]Department of Electrical Engineering, University of Engineering and Technology (UET), Lahore 39161, Pakistan
[2]College of Engineering & Applied Sciences, American University of Kuwait (AUK), Safat 13034, Kuwait

Corresponding author: Ghulam Amjad Hussain (ghussain@auk.edu.kw)

This work was supported by the Kuwait Foundation for the Advancement of Sciences (KFAS), under Project PR18-18EO-01.

ABSTRACT The recent increase in electricity prices and the usage of single-phase induction motors (SPIMs) provide a stimulus for a focused research on energy-efficient optimization of SPIM load such as air-conditioners and refrigerators. Variable speed control of SPIM provides a promising way forward to reduce its power consumption. However, during variable speed operation under the popular constant V/f method, SPIM is required to operate at non-rated conditions. The operation of SPIM at non-rated conditions disturbs its symmetrical and balanced operation, thus degrading its efficiency. Moreover, soft-starting of SPIM at non-rated conditions is also challenging due to the resulting reduction in starting-torque. In this article, after a detailed analysis of SPIM energy-efficiency, an improved sensor-less optimal speed control strategy is developed to enable the symmetrical and balanced operation of SPIM at all the operating points over the entire speed-range to improve its performance. A novel algorithm, termed as the phase-shift algorithm, is also devised for efficient implementation of the proposed optimal speed control strategy. In addition, a unique framework for efficient soft-starting of SPIM at very low frequencies is also developed. The simulation-based results of the motor operated through the proposed phase-shift algorithm validate the energy-saving potential of the proposed control strategy.

INDEX TERMS Energy-efficient control, variable speed drives, speed-sensorless induction motor control, magnetic-field control, inrush current reduction, starting torque, pulsating torque, energy savings in HVAC.

NOMENCLATURE

α	Effective turns ratio of auxiliary winding to main winding
ω_e	Electrical angular speed
ω_s	SPIM synchronous angular velocity
ϕ	Windings current phase difference
ϕ_v	Windings voltage phase difference
τ_{load}	Load torque
E_{ba}	Backward voltage of magnetizing branch of the auxiliary winding
E_{bm}	Backward voltage of magnetizing branch of the main winding
E_{fa}	Forward voltage of magnetizing branch of the auxiliary winding
E_{fm}	Forward voltage of magnetizing branch of the main winding
E_{mb}	Backward induced electromotive force of the main winding
E_{mf}	Forward induced electromotive force of the main winding
I_a	Auxiliary winding current
I_m	Main winding current
P_{out}	Output power
R_2	Rotor resistance referred to stator
R_{1a}	Auxiliary winding resistance
R_{1m}	Magnetizing reactance
R_{1m}	Main winding resistance
s	Slip
T_e	Electromagnetic torque
T_p	Peak torque
V_a	Auxiliary winding voltage

The associate editor coordinating the review of this manuscript and approving it for publication was Pinjia Zhang.

V_m Main winding voltage
X_2 Rotor reactance referred to stator
X_{1a} Auxiliary winding leakage reactance
X_{1m} Main winding leakage reactance
Z_a Auxiliary winding impedance
Z_m Main winding impedance

I. INTRODUCTION

Sinlge-phase induction motors (SPIMs) are widely used for domestic, household and low-power industrial purposes such as in heating, ventilation and air-conditioning (HVAC) systems. Although, the performance of these motors is worse than polyphase induction motors, SPIMS are cost effective and require less maintenance. Therefore, they are more feasible for low power applications. SPIMs have a huge starting inrush current, leading to a voltage dip in the power system whenever these motors are started [1]. Furthermore, the operation of these motors is feasible only on high wattage solar cells due to the requirement of substantial inrush current [2]. As SPIM-based load is the major load on any utility, there exists a huge potential for saving electricity by improving its energy-efficiency during starting and operating/running modes. Speed control of SPIM offers an opportunity to significantly increase the energy-savings [3]. For example, 50% of energy savings result from just 20% reduction in speed [4]. However, the research on energy-efficient sensor-less speed control of SPIM is not so rich, because its speed-control is inflexible as compared to that of the three-phase induction motor [5]–[7].

Unlike three-phase induction machines, the magnetic field inherently formed inside SPIM is not circular, i.e. not uniformly distributed in the air-gap. The elliptical and non-circular magnetic fields formed in SPIM result in significant backward rotating fields that heavily degrade its torque and efficiency [8]. Maximum average starting and operating torques are developed by SPIM when there exists quadrature and balance between main and auxiliary currents, which, in turn, produces a uniform circular rotating magnetic field in SPIM [9]. Therefore, in conventional SPIMs suitable start and run capacitors are inserted in series with the auxiliary winding to produce this quadrature between the main and auxiliary currents. However, these start and run capacitors are designed to generate circular rotating fields in SPIM at specific operating points, usually at the rated-load, and the field in SPIM at operating points other than the rated-conditions is elliptical [10]. On the contrary, energy-efficient speed-control of SPIM requires continuous operation at varying non-rated conditions and speed, with a continuously sweeping operating point. The variable speed operation of SPIM at these non-rated conditions leads to the formation of elliptical/non-circular magnetic fields and seriously degrades its efficiency [11]–[13]. Therefore, emphasis must be placed on symmetrical and balanced operation of SPIM at all operating points for energy efficient variable speed operation [14].

However, SPIMs have asymmetrical windings inherently, making it challenging to balance the respective currents during variable speed operation using conventional techniques. Furthermore, the main and auxiliary impedances vary dramatically from the starting to operating mode at a specific operating frequency [15]. In particular, these impedances vary with the changes in operating point and frequency as well. This variation disturbs the orthogonality and the balance between the main and auxiliary currents, leading to the degradation of its performance by causing the formation of elliptical fields during variable speed operation. During soft-starting at non-rated low-frequencies, the starting period is delayed and the resulting degradation of starting torque caused by elliptical fields at non-rated starting conditions can potentially stall the motor.

A well-known technique to improve the energy efficiency of SPIM is stator voltage control method [16], [17]. Similarly, there have also been studies on optimal design of SPIM for maximum efficiency on rated-conditions. However, these studies and proposed techniques are viable only in a small speed range and thus do not leverage the maximum energy-saving potential available through variable speed operation. SPIM energy-efficiency maximization techniques have also been proposed for variable speed operation [18]. These techniques minimize the electrical losses by adjusting the phase-difference ϕ between main and auxiliary currents. However, the adjustment of ϕ alters the efficient balanced and symmetrical operation of SPIM. Moreover, these techniques optimize SPIM efficiency at specific operating points, such as at a particular slip for a particular operating frequency, thus degrading its performance where a continuous efficient variable speed operation is indispensable. This requirement of existence of specific operating conditions for efficiency optimization also renders these techniques unsuitable for soft-starting.

Similarly, two phase operation of SPIM has also been shown to improve its efficiency at rated conditions [19]. However, these techniques do not address the resulting degradation in efficiency of SPIM when it operates far from rated operating point during variable speed operation. The techniques based on electronic adjustment of a fixed value capacitor also fail to maintain circular magnetic fields inside SPIM, since they do not take into account the variation in main and auxiliary impedances during starting and operating modes, and with changing operating-conditions [20].

Furthermore, during variable speed operation, the vector control strategies also fail to produce a perfect circular rotating magnetic field inside SPIM with asymmetrical windings [27]. These vector control strategies are highly dependent on precise sensor inputs and require expensive high-precision sensors for their implementation. The vector control strategies are highly computationally expensive and require dedicated digital signal processing- (DSP) enabled processors for their implementation. Moreover, due to the requirement of precise sensor inputs, these techniques are highly dependent on system state and therefore result in

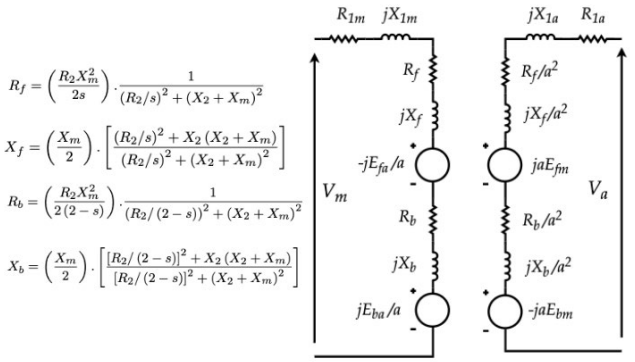

FIGURE 1. Double revolving field theory model of SPIM.

unstable operation under mild to sudden disturbances in the system.

In this article, after a detailed analysis of SPIM efficiency, sensor-less and computationally-efficient phase-shift algorithm is developed for energy-efficient operation of SPIM under the constant V/f speed control method. The phase-shift algorithm ensures the formation of circular magnetic fields inside SPIM by enabling its balanced and symmetrical operation at all operating points during starting and operating modes over the entire speed range. A unique framework for increasing the starting torque at low-frequencies is also formulated. This framework enables the soft-starting of SPIM at very low frequencies. Incorporating the proposed optimal control will improve the SPIM performance in three ways: energy saving with continuous variable speed operation, efficient power consumption with proposed SPIM efficiency optimization control and energy saving with soft-starting. This has not been reported so far.

The rest of this article is organized as follows. Maximum efficiency analysis is presented in section II. Section III defines the optimal control conditions for energy-efficient variable speed operation. In section IV, the phase-shift algorithm for the proposed optimal control is developed. The simulation-based implementation is discussed in sections V and VI. The results are discussed and the efficiency improvement of the proposed optimal control is compared with conventional techniques in section VII. Finally, a conclusion is given in section VIII.

II. DEPENDENCY OF MAXIMUM EFFICIENCY OF SPIM

A. MAXIMUM EFFICIENCY CONDITIONS

The equivalent model of SPIM with asymmetric main and auxiliary windings based on the Double Revolving Field theory [22] is given in Fig. 1. The model is obtained by simplifying the basic model of a SPIM and reducing the shunt elements ($0.5R_2/s$ and $0.5X_m$) into an equivalent series branch. According to this model, the average electromagnetic torque T_{em} developed by the SPIM having main and auxiliary windings in space quadrature is given by (1). The peak electromagnetic torque T_p is given by (2).

$$T_{em}.w_s = \left[I_m^2 + (\alpha I_a)^2\right]\left(R_f - R_b\right) + 2\alpha I_a I_m \left(R_f + R_b\right)\sin(\phi) \quad (1)$$

$$T_p.w_s = \left[\left(I_m^4 + (\alpha I_a)^4 + 2\left(\alpha I_a I_m\right)^2 \cos(2\phi)\right).\left[\left(R_f - R_b\right)^2 + \left(X_f - X_b\right)^2\right]\right]^{\frac{1}{2}} \quad (2)$$

1) PHASE ANGLE CONTROL FOR MAXIMUM ENERGY EFFICIENCY

The forward impedance, $R_f + jX_f$, and the backward impedance, $R_b + jX_b$, in the SPIM model are shown on the equivalent circuit, which depend upon R_2, X_m and s.

The voltages across the main and auxiliary winding (V_m and V_a respectively) can be related to the main and auxiliary windings currents through SPIM impedances as given by the Double Revolving Field theory based equivalent circuit of SPIM, as shown in Fig. 1. The main and auxiliary voltages can therefore be given as:

$$\boldsymbol{V_m} = \boldsymbol{I_m} Z_1 + \boldsymbol{I_a} Z_2 \quad (3)$$

$$\boldsymbol{V_a} = \boldsymbol{I_m} Z_4 + \boldsymbol{I_a} Z_3 \quad (4)$$

where;

$$Z_1 = R_{1m} + R_f + R_b + j\left(X_{1m} + X_f + X_b\right) = a_1 + jb_1 \quad (5)$$

$$Z_2 = -j_a\left[\left(R_f - R_b\right) + j\left(X_f - X_b\right)\right] = a_2 + jb_2 \quad (6)$$

$$Z_3 = \left[R_{1a} + \alpha^2(R_f + R_b)\right] + j\left[X_{1a} + \alpha^2\left(X_f + X_b\right)\right] = a_3 + jb_3 \quad (7)$$

$$Z_4 = j\alpha\left[\left(R_f - R_b\right) + j\left(X_f - X_b\right)\right] = a_4 + jb_4 \quad (8)$$

Solving (3) and (4) for $\boldsymbol{I_m}$ and $\boldsymbol{I_a}$, we get;

$$\boldsymbol{I_m} = \left(\boldsymbol{V_m} Z_3 - \boldsymbol{V_a} Z_2\right)/Z_d \quad (9)$$

$$\boldsymbol{I_a} = \left(\boldsymbol{V_a} Z_1 - \boldsymbol{V_m} Z_4\right)/Z_d \quad (10)$$

where

$$Z_d = Z_1 Z_3 - Z_2 Z_4 \quad (11)$$

As ϕ is the phase-difference between $\boldsymbol{I_m}$ and $\boldsymbol{I_a}$, it can be represented as the difference between the phase angles of numerator terms in (9) and (10):

$$\phi = \angle n_1 - \angle n_2 \quad (12)$$

where

$$n_1 = \boldsymbol{V_m} Z_3 - \boldsymbol{V_a} Z_2 \;;\; n_2 = \boldsymbol{V_a} Z_1 - \boldsymbol{V_m} Z_4$$

In this work, the main voltage is considered to be the reference with $\boldsymbol{V_m} = V_m \angle 0°$, and the auxiliary voltage can be represented as, $\boldsymbol{V_a} = V_{aR} + jV_{aI}$, with V_{aR} and V_{aI} as real and imaginary parts, respectively.

According to (12), to calculate ϕ, $\angle n_1$ and $\angle n_2$ are also derived in terms of SPIM parameters and are given as:

$$\angle n_1 = \tan^{-1}\left[\frac{V_m b_3 - V_{aI} a_2 - V_{aR} b_2}{V_m a_3 - V_{aR} a_2 + V_{aI} b_2}\right] \quad (13)$$

$$\angle n_2 = \tan^{-1}\left[\frac{V_{aR}b_1 + V_{aI}a_1 - V_m b_4}{V_{aR}a_1 - V_{aI}b_1 + V_m a_4}\right] \quad (14)$$

For $\phi = 90°$, the ratio of $\boldsymbol{I_a}$ to $\boldsymbol{I_m}$ must produce an imaginary result:

$$\frac{\boldsymbol{I_a}}{\boldsymbol{I_m}} = \frac{\boldsymbol{V_a}Z_1 - \boldsymbol{V_m}Z_4}{\boldsymbol{V_m}Z_3 - \boldsymbol{V_a}Z_2} = j\zeta \quad (15)$$

By multiplying both sides of the (15) with the denominator, using the (9) and (10) to express currents in terms of voltages, collecting real and imaginary parts, and separating, we get the following result:

$$V_{aR} - V_{aI}b_1 - V_m a_4 = \zeta\left[V_{aI}a_2 + V_{aR}b_2 - V_m b_3\right] \quad (16)$$
$$V_{aR}b_1 + V_{aI}a_1 - V_m b_4 = \zeta\left[V_m a_3 - V_{aR}a_2 + V_{aI}b_2\right] \quad (17)$$

Through tedious algebraic manipulation of the above equation, we get:

$$V_{aR}^2 + V_{aI}^2 + PV_{aR} + QV_{aI} + R = 0 \quad (18a)$$

where

$$P = \frac{V_m}{T}(a_1a_3 + a_2a_4 + b_1b_3 + b_2b_4) \quad (18b)$$
$$Q = \frac{V_m}{T}(a_1b_3 + a_2b_4 - a_3b_1 - a_4b_2) \quad (18c)$$
$$R = \frac{-V_m^2}{T}(a_3a_4 + b_3b_4) \quad (18d)$$
$$T = -(a_1a_2 + b_1b_2) \quad (18e)$$

Again, through algebraic manipulation of (18), we get:

$$V_{aI\,1,2} = \frac{-Q\left(R + V_a^2\right)}{P^2 + Q^2} \pm \frac{1}{P^2 + Q^2}\left\{Q^2\left(R + V_a^2\right)^2 - \left(P^2 + Q^2\right)\left[V_a^4 + V_a^2\left(2R - P^2\right) + R^2\right]\right\}^{\frac{1}{2}} \quad (19)$$

$$V_{aR1,2} = \pm\sqrt{V_a^2 - V_{aI\,1,2}^2} \quad (20)$$

$$V_a = V_{aR1,2} + jV_{aI\,1,2} \quad (21)$$

The auxiliary phase can be calculated through inverse tangent:

$$\phi_v = \tan^{-1}\left(\frac{V_{aI}}{V_{aR}}\right) \quad (22)$$

By solving the above system of equations simultaneously, (22) gives the solution of ϕ_v for $\phi = 90°$. Thus, the value of ϕ_v for $\phi = 90°$ depends on the SPIM parameters, operating frequency and speed.

2) VOLTAGE CONTROL FOR MAXIMUM ENERGY EFFICIENCY

In conventional SPIMs, start and run capacitances are designed to minimize torque pulsations at a specific operating point, usually at the rated-load condition. This strategy results in the sacrifice of SPIM performance (efficiency and torque) at other operating points. When $\phi = 90°$ and the two currents, I_m and I_a are balanced, the formation of circular rotating magnetic field in SPIM results in the elimination of torque pulsations. The analysis of (2) shows that the torque pulsations in SPIM are eliminated at any operating point if the following condition holds:

$$\cos(2\phi) = \frac{-I_m^4 + (\alpha I_a)^4}{2\left(\alpha I_a I_m\right)^2} \quad (23)$$

The above equation boils down and constrains the magnitudes of $\boldsymbol{I_m}$ and $\boldsymbol{I_a}$ to the following condition:

$$\left(\frac{I_m}{\alpha I_a}\right)^2 + \left(\frac{\alpha I_a}{I_m}\right)^2 = 2 \quad (24)$$

For $\phi = 90°$, since I_m and I_a in the above equation are real numbers, the only solution to this equation is $I_m = \pm\alpha I_a$. Therefore, using (3) and (4), the voltages V_m and V_a can be related as:

$$V_a = |\boldsymbol{V_a}| = V_m\left|\frac{Z_3 + \alpha Z_4}{\alpha Z_1 + Z_2}\right| \quad (25)$$

$$V_a = V_m\left[\frac{(a_3 + \alpha a_4)^2 + (b_3 + \alpha b_4)^2}{(a_2 + \alpha a_1)^2 + (b_2 + \alpha b_1)^2}\right]^{\frac{1}{2}} = V_m * k \quad (26)$$

where

$$k = \left[\frac{(a_3 + \alpha a_4)^2 + (b_3 + \alpha b_4)^2}{(a_2 + \alpha a_1)^2 + (b_2 + \alpha b_1)^2}\right]^{\frac{1}{2}} \quad (27)$$

Substituting $\phi = 90°$ in (1), the average electromagnetic torque reaches its maximum value for the same I_m and I_a. This means less current is drawn by SPIM to meet the same load torque. Hence, energy-efficiency under a specific load is maximized by reducing current per torque.

If $\phi = 90°$ and the above condition, $V_a = V_m * k$, holds, circular rotating magnetic field is formed inside SPIM at any operating point and torque pulsations are eliminated, thus maximizing the efficiency of SPIM during variable speed operation.

When $\phi = 40°$, the elliptical rotating field which is the source of torque pulsations is shown in Fig. 2a. When $\phi = 90°$, and the two currents are balanced, the resultant circular rotating magnetic field is shown in Fig. 2b.

III. ENERGY-EFFICIENT VARIABLE SPEED CONTROL

As discussed in the previous section, (22) and (26) must be satisfied for maximum efficiency operation of SPIM. The value of k in (26) depends on SPIM impedances, operating conditions and rotational speed, that are, in turn, dependent on the operating frequency and load-conditions. Furthermore, in this article, as the variable speed control of SPIM is implemented using the constant V/f method, V_m is also adjusted with varying frequency. According to (26), this proves the dependence of optimal V_a on the operating frequency. Therefore, for balanced and symmetrical variable speed operation of SPIM, V_a must be updated according to (26) with operating frequency and speed. Similarly, according to the analysis in the previous section, the optimal ϕ_v also depends on operating frequency and must be adjusted accordingly.

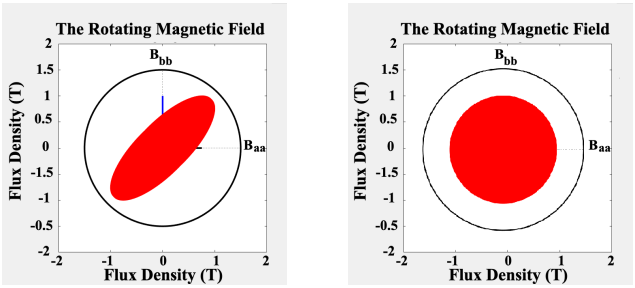

(a) Rotating magnetic field in SPIM under unbalanced operation.

(b) Rotating magnetic field in SPIM under balanced and symmetrical operation.

FIGURE 2. Rotating magnetic field in SPIM.

In this article, a closed loop control of SPIM is implemented to evaluate the efficiency improvement of the proposed strategy at varying load-conditions. However, SPIMs are required to operate at a constant load in most industrial applications. The operating speed remains constant for a given load at a particular operating frequency and can be calculated using the torque speed characteristics of the SPIM under the proposed optimal control technique. This eliminates the need of speed sensor and a look up table technique is implemented using the proposed optimal control strategy which is discussed in detail in section VII.

The sensor-less scalar implementation eliminates the need of various high-cost sensors, like high-precision current and voltage sensors, rotor speed and rotor position sensors, that are required for the implementation of conventional vector control techniques. Moreover, the proposed sensor-less technique makes the optimal control less-dependent on the system state, thus making it robust to the disturbances in the system compared to similar sensor-based techniques, like vector control strategies for SPIM speed control.

The two primary weaknesses associated with the recent variants of the constant V/f method [3]–[21] can be summarized as follows:

1. These techniques produce a circular rotating magnetic field inside SPIM for a very narrow range of operating frequencies/speeds and fail to produce circular rotating magnetic field as the operating point of SPIM moves far away from its rated operating point during its variable speed operation.

2. During the fixed speed operation of SPIM at a specific frequency usually near the rated conditions, these techniques produce circular rotating magnetic field inside it at specific fixed starting and operating point. These techniques again fail to produce circular rotating magnetic field during the transition of operating point from starting to operating condition at a fixed operating frequency.

The two primary causes for the weaknesses associated with these variants of the constant V/f method can be summarized as follows:

1. During variable speed operation, the main and auxiliary impedances of SPIM vary dynamically and asymmetrically with its varying operating point.

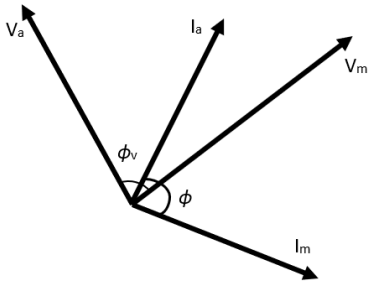

FIGURE 3. Voltage and current phasors of SPIM.

2. During constant speed operation at a particular frequency, these impedances change dynamically and asymmetrically as the operating point of SPIM transitions from starting to operating condition.

These factors become more and more significant as the SPIM is started and operated at conditions farther away from its rated operating point. Therefore, these variants of the constant V/f method fail at conditions farther away from its rated operating point, and thus degrade its circular rotating magnetic field and energy efficiency.

A. OPERATING MODE

According to the double revolving field theory, the phase difference ϕ manipulates the magnetic field inside SPIM. The phasor diagram of various SPIM voltages and currents is shown in Fig. 3. For the generation of circular rotating magnetic field inside SPIM, ϕ must be maintained at 90° during the starting and operating conditions.

For variable speed operation of conventional SPIMs, as the operating frequency is varied, the SPIM impedances change and the operating point moves away from the rated operating point. This results in the distortion of rotating magnetic field increasing torque pulsations. Therefore, lowering the operating frequency of SPIM for variable speed operation seriously degrades its efficiency. Moreover, for SPIM operation at a fixed frequency, the main and auxiliary impedances vary drastically from starting to operating mode. The auxiliary impedance also varies significantly with load-conditions. These disturbances also contribute to the unsymmetrical and unbalanced operation of SPIM.

Therefore, to maintain quadrature between main and auxiliary currents ($\phi = 90°$), as ϕ is obtained as a function of ϕ_v in the previous section, ϕ_v must be updated continuously to account for these sustained variations in SPIM impedances with operating frequency and conditions. In addition, for the generation of circular magnetic field inside SPIM, the condition expressed by (26) must also be satisfied. Therefore, it becomes necessary to adjust V_a with varying frequency, speed and load-conditions.

B. STARTING MODE

Soft-starting of SPIM at low-frequencies can substantially reduce the inrush current and thus increase energy-savings. However, when SPIM is started at very low frequencies,

the starting time is delayed. The torque pulsations occurring during the transition from starting to operating condition due to unbalanced operation significantly reduce its developed torque. In most industrial applications, the load torque increases linearly with starting speed and the reduction in developed torque caused by elliptical fields during starting results in increased I_m and ultimately stalls the motor. In other words, soft-starting of SPIM at low frequencies results in a considerable divergence of operating point from the rated conditions and seriously degrades the starting torque.

A symmetrical and balanced starting operation of SPIM enabled by optimal ϕ_v and V_a control according to (22) and (26) results in a significant increase in starting torque at low-frequencies. This substantial increase in starting torque results in decreased I_m for a specific load and increases starting efficiency.

IV. PHASE-SHIFT ALGORITHM FOR IMPLEMENTATION OF EFFICIENCY OPTIMIZATION CONTROL

A. CHALLENGES IN IMPLEMENTATION

As discussed, optimal ϕ_v and V_a control is needed for energy-efficient variable speed operation of SPIM. Thus, the implementation of the proposed efficiency optimization control requires real-time generation of suitable variable phase, variable frequency and variable magnitude voltage waveforms. However, to the best of the authors' knowledge, there does not exist a dedicated technique in the literature for sinusoidal pulse width modulation (SPWM)-based real-time generation of variable phase voltage waveform. In conventional techniques, for the digital synthesis of a variable frequency and variable magnitude sinusoidal voltage waveform, sine lookup table is generated corresponding to SPWM switching pattern for a specific frequency. These techniques use pre-stored sine lookup tables or reference values for the generation of variable frequency variable voltage SPWM [23]–[25]. This is memory intensive and compromises the required precise frequency and voltage control [26].

The dependence of optimal phase ϕ_v on SPIM parameters and operating conditions, in addition to frequency, necessitates the formulation of a novel real-time SPWM generation framework. Furthermore, as modulation index of SPWM is used to efficiently control V_a for balanced operation, the generated sine lookup tables for a specific frequency SPWM switching pattern will vary according to SPIM parameters and operating conditions. This provides another justification for not using the pre-stored sine lookup tables or reference values for variable frequency, variable phase and variable magnitude SPWM switching pattern generation.

Therefore, for a precise ϕ_v and V_a control, real-time calculation of sine look up tables is required. However, the calculation of sine of a given value involves multiplication operations, that are computationally expensive to be implemented on micro-controllers without a hardware multiplier. So, using conventional techniques, a dynamic real-time control of ϕ_v and V_a is impossible.

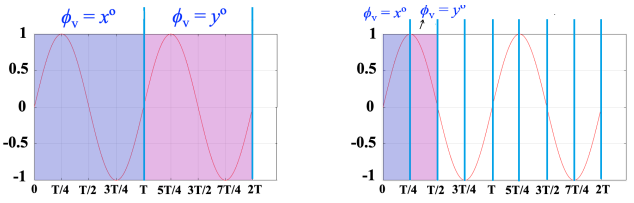

(a) ϕ_v update in discrete time-periods under conventional techniques.

(b) ϕ_v update in discrete segments under the phase-shift algorithm.

FIGURE 4. ϕ_v update in discrete time-periods under conventional techniques vs. under the proposed phase-shift algorithm for optimal control.

To account for the use of pre-stored reference values and the associated computational cost, in conventional techniques, a change in ϕ_v is possible only in discrete time-periods/cycles of voltage waveform and magnetic field. So a change in ϕ_v requested in current time-period/cycle is implemented in the following discrete time-period/cycle of auxiliary voltage waveform, thus delaying the phase-response to the subsequent magnetic field rotation as shown in Fig. 4a. Similarly, in conventional techniques, the voltage V_a for variable speed operation is also updated in discrete time periods.

As SPIM is started/operated at low-frequencies of the order of 0.5Hz, the time-period required for one complete magnetic field rotation is significantly delayed. In most of the industrial applications, the load increases exponentially with SPIM speed at the starting along with the induction of huge starting inrush current. These factors necessitate prompt update of ϕ_v and V_a according to optimal efficiency control before the start of the discrete magnetic field or auxiliary voltage cycle. If ϕ_v and V_a are not adjusted dynamically to maintain quadrature and balance between currents, the resulting degradation in the available starting torque stalls the motor. Similarly, during operating conditions at medium and low frequencies, delayed optimal ϕ_v and V_a update results in torque degradation, which makes the SPIM operation inefficient.

In this article, for real-time control of ϕ_v and V_a, it is proposed to divide one complete magnetic field rotation by the partition of corresponding auxiliary voltage waveform into a desired number of n segments. In the following section, the phase-shift algorithm is developed to provide ϕ_v and V_a control within the segment to promptly account for the disturbances in quadrature during starting and operating conditions. In this way, ϕ_v and V_a can be adjusted online for the formation of circular magnetic field within discrete segments without waiting for the whole rotation to complete as shown in Fig. 4b.

B. CONCEPT EXPLORATION

As discussed in the previous section, a dynamic real-time control of ϕ_v and V_a is required for energy-efficient variable speed operation of SPIMs. However, this dynamic control makes the input voltage waveform V_a non-sinusoidal at low-frequencies. This non-sinusoidal voltage waveform is difficult to be synthesized at low frequencies using conventional techniques.

Therefore, in this section, the phase-shift algorithm for dynamic real-time control of phase-shift, voltage and frequency is developed. The phase-shift algorithm generates the sine lookup tables for the two variable phase, variable frequency and variable magnitude waveforms in real-time based on the SPWM technique. The SPWM switching pattern generated by the phase-shift algorithm is used for driving the corresponding switches of two isolated H-Bridge inverters to generate the output main and auxiliary voltage waveforms as shown in Fig. 5. Using the phase shift algorithm, the waveforms V_m and V_a are manipulated to control the operating parameters of the SPIM as discussed in section II.

In the phase-shift algorithm, one complete time-period T of each waveform V_m and V_a is divided into segments S. Each segment is of equal time duration. If a waveform is divided into n segments.

$$S = n \tag{28}$$
$$T_s = T/n \tag{29}$$

where S represents the total no. of segments in T and T_s is the time duration of one segment. If V_m and V_a are divided individually into 4 segments, each segment is known as a quadrant;

$$S_m = 4 \tag{30}$$
$$T_{sm} = T_m/4 \tag{31}$$
$$S_a = 4 \tag{32}$$
$$T_{sa} = T_a/4 \tag{33}$$

where S_m represents the total number of segments in which waveform V_m is divided, T_{sm} is the time duration of V_m's one segment, and T_m is the time period of V_m. Similarly, S_a represents total number of segments in which waveform V_a is divided, T_{sa} is the time duration of V_a's one segment and T_a is the time period of V_a. $Q1_m$, $Q2_m$, $Q3_m$ and $Q4_m$ represent the 1st, 2nd, 3rd and 4th quadrants of V_m respectively. $Q1_a$, $Q2_a$, $Q3_a$ and $Q4_a$ represent the 1st, 2nd, 3rd and 4th quadrant of V_a respectively. The corresponding waveforms are plotted in Fig. 6a. In phase shift algorithm, the voltage amplitude and frequency of each of the waveforms V_m and V_a is controlled independently and dynamically in each quadrant. Moreover, the phase shift between the two waveforms V_m and V_a can be varied dynamically in each quadrant as well.

Fig. 6b represents the output waveform obtained through the phase shift algorithm with adjustable phase difference in each quadrant. By adjusting n, using the phase shift algorithm, a waveform can be divided into desired number of segments. The phase difference between the two waveforms, as well as the voltage amplitude and frequency of individual waveform can be independently adjusted in each segment to obtain the desired output characteristics.

C. IMPLEMENTATION

The phase-shift algorithm generates the switching pattern of the switches S1 through S8 using SPWM technique as shown in Fig. 5. To generate the sine lookup tables for the output SPWM pattern corresponding to different frequencies, Cordic Algorithm with improved rotation strategy is used [27]. Cordic Algorithm is an iterative method that calculates the sine of a value using addition, subtraction and shift operations. Conventional methods of sine calculation use multiplication operation, which is computationally expensive. Improved cordic algorithm calculates the sine of values within a couple of clock cycles of the microcontroller. Therefore, in order to reduce the time required for generating various sine lookup tables for a dynamic response, improved cordic algorithm will be used and the corresponding function will be denoted as c_sin().

For an output waveform W with time period T, the corresponding SPWM generation will consist of the following parameters;

$$T = 1/f \tag{34}$$
$$t_s = 1/f_s \tag{35}$$
$$n_s = T/t_s \tag{36}$$
$$ph_i = 360°/n_s \tag{37}$$

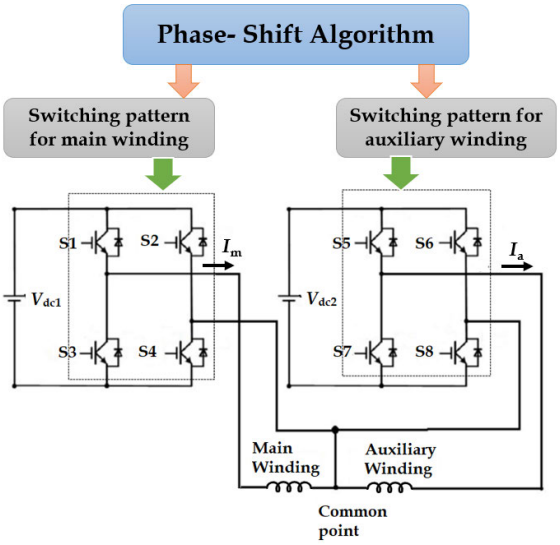

FIGURE 5. Switching pattern generation using the phase-shift algorithm for efficient variable speed operation of SPIM.

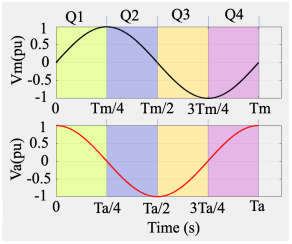

(a) Division of V_m and V_a into discrete segments for dynamic phase-control.

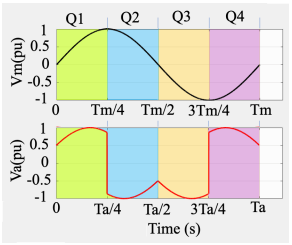

(b) Dynamic phase control of input voltage using the phase-shift algorithm. V_a leads V_m by 30° in Q1 and Q3, and by 150° in in Q2 and Q4.

FIGURE 6. Dynamic phase control of input voltage waveform using the phase-shift algorithm.

where f is the frequency of the output waveform generated through phase shift algorithm, f_s is the sampling frequency of the SPWM pattern, t_s is the time duration of one SPWM sample, n_s represents total number of SPWM samples in T and ph_i is the phase increment for each SPWM sample.

In the phase shift algorithm, the sine lookup table cannot have any negative value because the corresponding values of sine look up table are fed into Microcontroller's timer register to adjust the duty cycle of each output PWM signal to form SPWM output. Therefore, another array, *switch_toggle*, is formed which keeps the record of the occurrences of the negative cycle of the output waveform W. For each element in sine look up table, there is a corresponding element in *switch_toggle* array. The element is either '0' or '1' depending on the polarity of the output waveform W it is representing. The element is:

0: if the corresponding element in the sine lookup table relates to the positive cycle of the output waveform W
1: if the corresponding element in the sine lookup table relates to the negative cycle of the output waveform W

D. CODE

The sine lookup table and the *switch_toggle* array can be found using the for loop as follows:

for $i = 1: n_s$
  $\left(c\_sin\left(\left(\frac{\pi}{180} * ph_i * i\right) + \left(\varphi[i] * \frac{\pi}{180}\right)\right)\right) = \gamma$
  if $(\gamma \geq 0)$
    $sin\_LUT\ (i) = \beta * \gamma$
    $switch\_toggle\ (i) = 0$
  end
  if $(\gamma < 0)$
    $sin\_LUT\ (i) = -\beta * \gamma$
    $switch\_toggle\ (i) = 1$
  end
end

In the above code, φ is a variable containing the phase-shift to be inserted in the output waveform. β is the modulation index which ranges from 0 to 1. *sin_LUT*() is the array containing the sine lookup table for the corresponding output waveform.

When *switch_toggle* $= 0$, path 1 of the corresponding H-Bridge will be active and path 2 will be inactive. When *switch_toggle* $= 1$, path 1 will become inactive and path 2 will become active, as shown in Fig. 7a and Fig. 7b, respectively.

E. FREQUENCY CONTROL

By adjusting the vaiable f in the above section, the sine lookup tables can be generated for corresponding output frequencies dynamically and efficiently. In the algorithm, f can be adjusted within fractions of 0.1 Hz, thereby allowing a precise speed control of SPIM. By increasing the SPWM sampling frequency, f_s, a precise sine output waveform can be generated even for higher frequencies. At lower end, phase shift algorithm can efficiently generate output waveforms of frequencies as low as 0.1 Hz. Therefore, the phase shift algorithm allows the SPIM to be operated at very low frequencies.

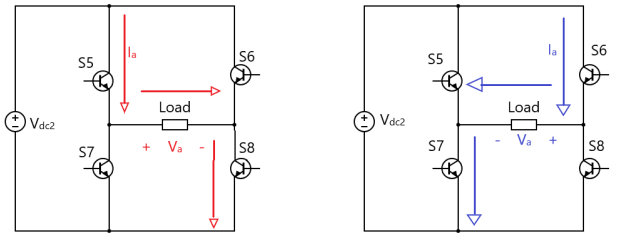

(a) Path 1 (positive cycle) of corresponding isolated H-Bridge.

(b) Path 2 (negative cycle) of corresponding isolated H-Bridge.

FIGURE 7. Load voltage during switching operations.

F. VOLTAGE CONTROL

In the above code, β is the modulation index and ranges from 0 to 1. By appropriately adjusting the modulation index, the magnitude of the output waveform can be controlled. This voltage control offered by the phase-shift algorithm is used for real-time optimal control of V_a according to (26).

For discrete segment based optimal voltage-control, a separate array, $\beta[n_s]$, can be created and segmented in the same fashion as sine lookup table.

G. PHASE-SHIFT CONTROL

In this section, the segment-wise phase control of a waveform is discussed. For the output waveform W with time period T, the corresponding sine lookup table, *sin_LUT*, and *swtich_toggle* array are:

$$sin\_LUT = [l_1\ l_2\ \ldots\ldots l_{n_t}]$$
$$switch\_toggle = [t_1\ t_2\ \ldots\ldots t_{n_t}]$$

where

$l_i = i^{th}$ element of *sin_LUT*
$t_i = i^{th}$ element of *switch_toggle*
n_t = total number of SPWM samples in time period T

Using the phase shift algorithm, this waveform is divided into n segments. The entries of the two arrays corresponding to each segment will be

$$e = n_t/n \tag{38}$$

where

e = number of entries corresponding to each segment

In order to shift the phase from one segment to another, the entries related to that particular section in both *sin_LUT* and *switch_toggle* array need to be replaced with the corresponding entries from sine lookup table and *switch_toggle* array of the phase shifted waveform, respectively.

Consider the sine lookup table and switch toggle array of the phase shifted waveform with phase shift of φ;

$$sin\_LUT\_\varphi = [l_{\phi 1}\ l_{\phi 2}\ \ldots\ldots l_{\phi n}]$$
$$switch\_toggle\_\varphi = [t_{\phi 1}\ t_{\phi 2}\ \ldots\ldots t_{\phi n}]$$

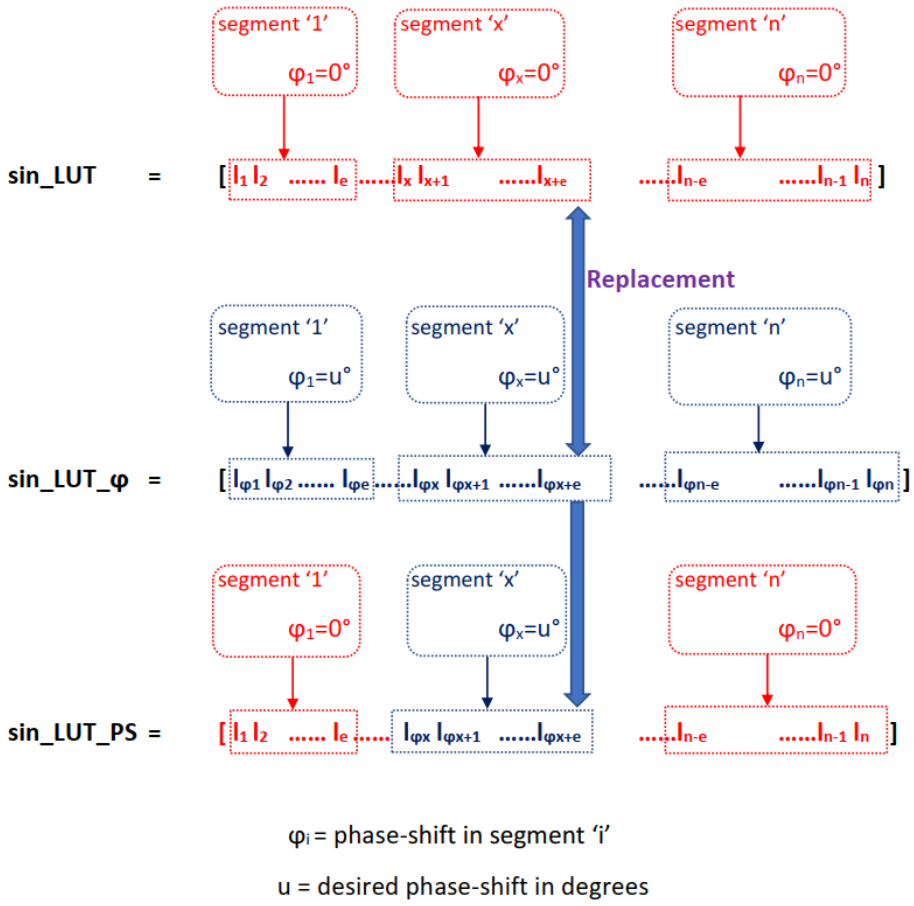

FIGURE 8. Replacement Operation for *sin_LUT* for dynamic phase update.

where $l_{\phi i} = i^{th}$ element of sin_LUT_φ

$t_{\phi i} = i^{th}$ element of $switch\_toggle\_\varphi$

To insert a phase shift of φ in segment x, the following entries of *sin_LUT* and *switch_toggle* arrays need to be replaced with the corresponding entries in sin_LUT_φ and $switch\_toggle\_\varphi$;

Entries of *sin_LUT* corresponding to section x

$$= l_x, l_{x+1}, \ldots\ldots\ldots l_{x+e}$$

Entries of *switch_toggle* corresponding to section x

$$= t_x, t_{x+1}, \ldots\ldots\ldots, t_{x+e}$$

Entries of sin_LUT_φ corresponding to section x

$$= l_{\phi x}, l_{\phi x+1}, \ldots\ldots\ldots, l_{\phi x+e}$$

Entries of $switch\_toggle\_\varphi$ corresponding to section x

$$= t_{\phi x} t_{\phi x+1} \ldots\ldots\ldots t_{\phi x+e}$$

The following entries corresponding to original waveform are replaced with the entries corresponding to the phase shifted waveform, with the arrow representing the replacement operation:

$$l_{\phi x} l_{\phi x+1} \ldots\ldots\ldots l_{\phi x+e} \Rightarrow l_x l_{x+1} \ldots\ldots\ldots l_{x+e}$$
$$t_{\phi x} t_{\phi x+1} \ldots\ldots\ldots t_{\phi x+e} \Rightarrow t_x t_{x+1} \ldots\ldots\ldots t_{x+e}$$

The sin lookup table and switch toggle arrays of the new phase-shifted waveform will be

$$sin\_LUT\_PS = [l_1 \ldots . l_{\phi x}\ l_{\phi x+1} \ldots . l_{\phi x+e} \ldots . l_{n_t}]$$
$$switch\_toggle\_PS = [t_1 \ldots . t_{\phi x}\ t_{\phi x+1} \ldots . t_{\phi x+e} \ldots . t_{n_t}]$$

For a phase shift of φ in any section, the above procedure needs to be repeated. The replacement of requisite segment in the corresponding sine lookup is demonstrated in Fig. 8. In practice, the phase shifted arrays are generated by adjusting the value of φ in code during real-time for the corresponding section, instead of calculating the arrays for phase shifted waveforms individually and then replacing the corresponding entries. The values of various arrays for the output waveform V_a as shown in Fig. 6a, are plotted in Fig. 9a. The corresponding PWM switching signals for real-time phase control generated by the phase-shift algorithm for V_a with $f_s = 10$kHz and $f = 50$Hz are shown in Fig. 9b.

V. SIMULATION-BASED IMPLEMENTATION

A. TEST SETUP

To leverage the maximum potential offered by the phase-shift algorithm, it is proposed to operate the SPIM as a capacitorless two phase asymmetric motor as shown in Fig. 10.

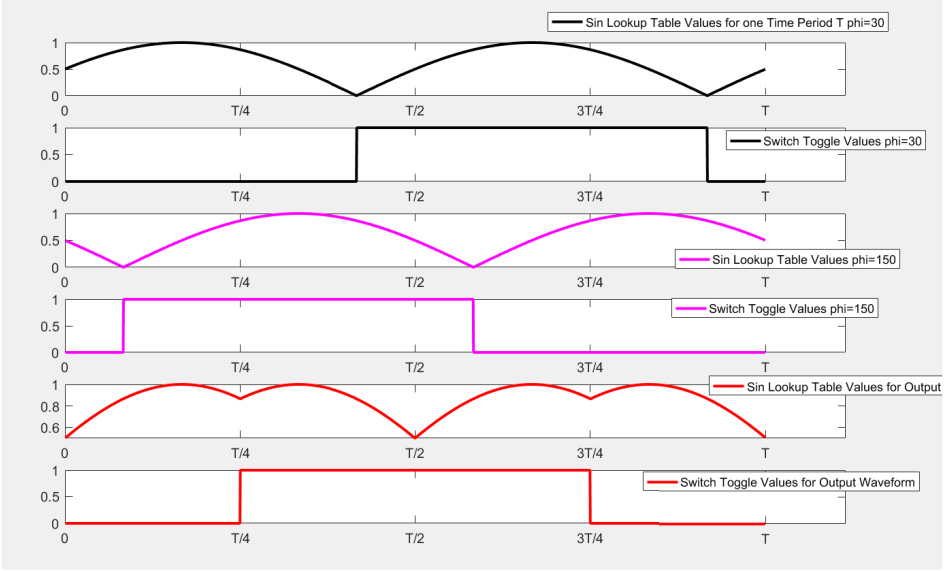

(a) Values of various arrays for output waveform V_a shown in Fig. 6b

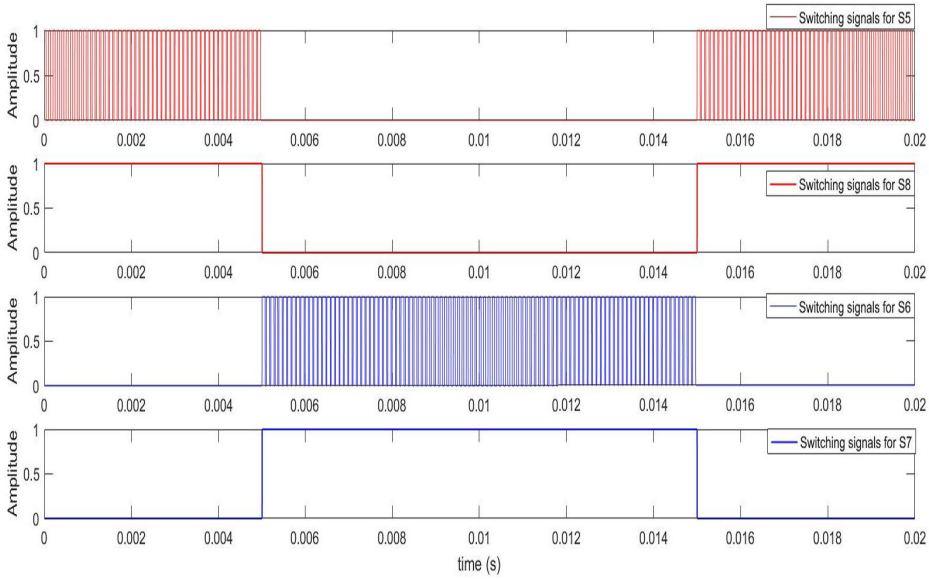

(b) Switching signals generated by the phase-shift algorithm for dynamic phase control with $f_s = 10$kHz, $f = 50$Hz and modulation index=0.8.

FIGURE 9. **Values of various arrays and corresponding switching signals generated by the phase-shift algorithm for dynamic phase-control.**

This mode of operation enables the simultaneous constant V/f control and optimal phase-control of SPIM. The constant V/f control is used to implement variable speed operation of SPIM. The optimal phase-shift control enables the optimal V_a and ϕ_v control for formation of circular magnetic field inside SPIM as discussed in section II. The simultaneous implementation of V/f control and optimal phase-control permits the energy-efficient symmetric and balanced variable speed operation of SPIM. This simultaneous implementation also enables the efficient soft-starting of SPIM at very low-frequencies based on the framework developed in the previous section.

The two-phase supply is obtained from a single-phase supply using a rectifier and two isolated H-Bridge inverters. The switching pattern of switches S1 through S8, as shown in Fig. 5, is generated by the phase-shift algorithm and implemented using the dual isolated H-Bridge inverter topology. As discussed in the previous section, the switching pattern is generated using the phase-shift algorithm so that the voltage amplitude, frequency and the phase-shift between V_m and V_a can be independently and dynamically controlled to implement the optimal V_a and ϕ_v control for energy-efficient variable speed operaiton.

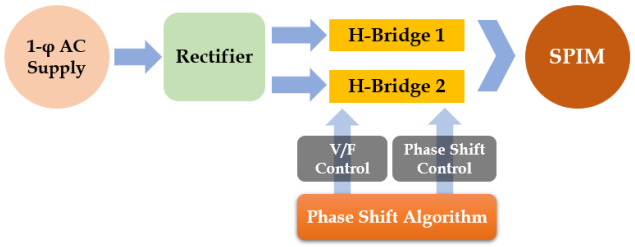

FIGURE 10. Two phase operation of SPIM under the phase-shift algorithm for efficient variable speed control.

The two DC link voltage sources V_{dc1} and V_{dc2}, shown in Fig. 5, must be isolated because most of the over-the-counter SPIMs have a common connection point between the main and auxiliary windings. In order to independently control the two windings, the DC links energizing the respective windings must be isolated.

In this layout, two full-bridge inverters are used instead of two half-bridge inverters because full-bridge inverters provide a comparatively more flexible and improved voltage control. In case of half-bridge inverters, the DC link voltage must be twice as high as that of the fundamental component of the motor input voltage, necessitating the use of additional transformer or DC-DC converter to achieve the required voltage level. In case of full-bridge inverters, output from the rectifier can be directly used to energize the inverters with the help of just one filtering capacitor. Moreover, two and three level waveforms can be generated in case of full-bridge inverters giving more flexibility to the designer of the motor drive to achieve desired characteristics.

The proposed technique and its implementation algorithm (phase-shift algorithm) is flexible and can be implemented using various inverter topologies. To reduce the cost of overall drive, this algorithm can be implemented using two two-switches-based half-bridge inverters without any modification to the implementation algorithm. For increased efficiency of the drive, the proposed technique can be implemented using multi-level topologies based on two four-switches-based full-bridge inverters. Similarly, further topologies can be investigated for the implementation of the proposed technique depending on the designer's requirements.

For soft-starting at very low-frequencies, the number of segments in the phase-shift algorithm, n, must be kept very large to account for the prolonged time-period of the input voltage waveform. A very large n enables dynamic update of ϕ_v and V_a at low-frequencies. For high operating frequencies n can be kept small to reduce the computational time and complexity.

B. CONSTANT V/f CONTROL

The constant V/f control is implemented to enable the variable speed operation of SPIM. To implement the constant V/f control, magnitude of $\boldsymbol{V_m}$ and frequencies of $\boldsymbol{V_a}$ and $\boldsymbol{V_m}$ are controlled by the phase-shift algorithm through the generation of suitable sine look up tables, switch toggle array and modulation index as discussed in the previous section. In this article, the modulation index is used to control the voltage magnitude.

TABLE 1. SPIM Parameters and Ratings.

Power	1 hp	L_{1m}	7.4 mH
V_{rated}	110V	L_{1a}	8.5 mH
f	60 Hz	L_m	0.1772 H
R_{1m}	2.02 Ω	C_{rated}	30 μF
R_{1a}	7.14Ω	C_{start}	300μF
α	1.18		

C. OPTIMAL PHASE-SHIFT CONTROL

The optimal phase-shift control is implemented to enable the optimal ϕ_v and V_a control for the symmetric and balanced operation of SPIM at varying frequencies and speeds. The phase-shift control also enables the efficient soft-starting of SPIM at very low frequencies. Using the phase-shift algorithm, the magnitude of $\boldsymbol{V_a}$ is controlled through the modulation index for optimal V_a control. The phase of $\boldsymbol{V_a}$ is controlled through the generation of suitable sine lookup tables as discussed in the previous section for optimal ϕ_v control.

VI. SIMULATION-BASED EVALUATION

In order to evaluate the proposed control strategy, a MATLAB/Simulink model is developed as shown in Fig. 11. The parameters of SPIM are given in the Table. 1. A feedback control system is developed to carry out the tests at varying frequencies with non-rated load conditions. The feedback control also provides the torque-speed characteristics of SPIM under the proposed optimal control over the entire frequency range. These torque-speed characteristics are then used to repeat the tests with a look up table-based control which is discussed in the next section. To evaluate the efficiency improvement of the proposed algorithm, simulations are repeated with the constant V/f control method for direct comparison of performance efficiency.

The test setup is developed as described in the previous section. However, the SPIM used in this test has discrete main and auxiliary windings, so the isolation between the DC links energizing the two full-bridge inverters is not needed. As shown in Fig. 11, the SPIM parameters are pre-stored in the optimal control block as input parameters. The optimal control block receives the operating frequency, speed and V_m during real-time. An algorithm is implemented in optimal control block which calculates the optimal V_a and ϕ_v based on the analysis in section II for balanced and symmetrical operation of SPIM. The ϕ_v and V_a for optimal control are then fed to the phase-shift algorithm module, which generates the switching signals for the two full-bridge inverters as described in section IV. The magnitude and phase of $\boldsymbol{V_a}$ are controlled to implement optimal ϕ_v and V_a control at the desired frequency.

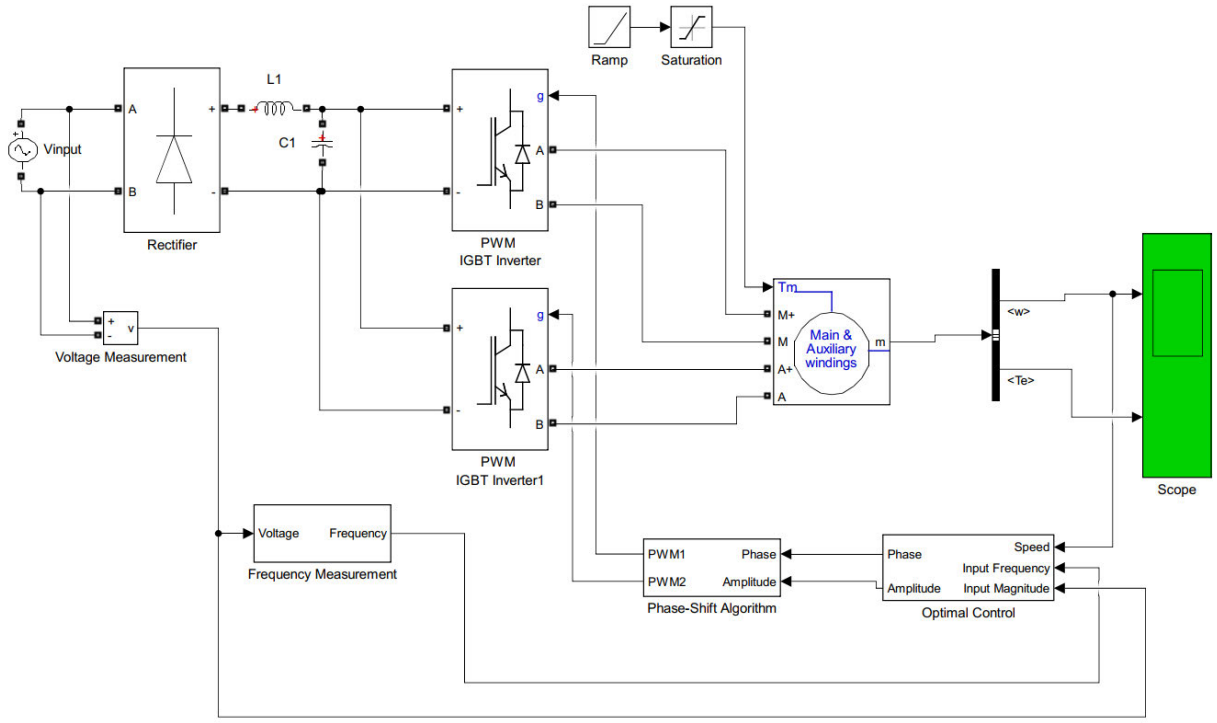

FIGURE 11. Test setup for the implementation of the proposed optimal strategy.

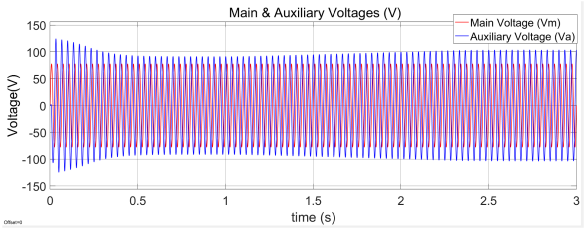

(a) Main and auxiliary voltages at $f = 30$ Hz under the proposed optimal control strategy.

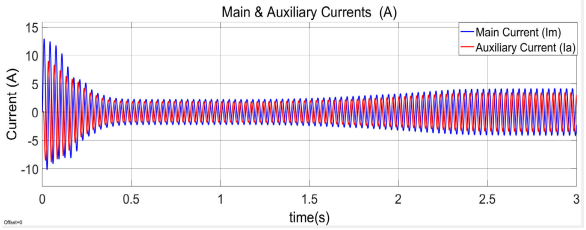

(b) Main and auxiliary currents at $f = 30$ Hz under the proposed optimal control strategy.

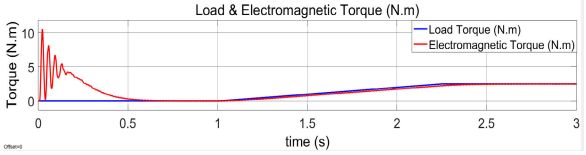

(c) Load and electromagnetic torque at $f = 30$ Hz under the proposed optimal control strategy.

FIGURE 12. Simulation-based results of SPIM operation under the proposed optimal control at $f = 30$ Hz.

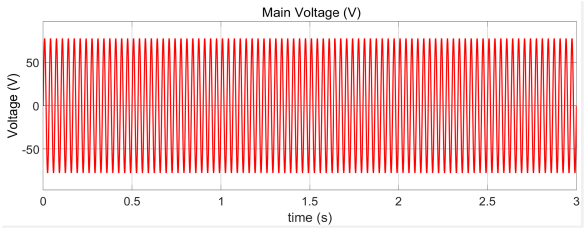

(a) Main voltage at $f = 30$ Hz under the constant V/f control method.

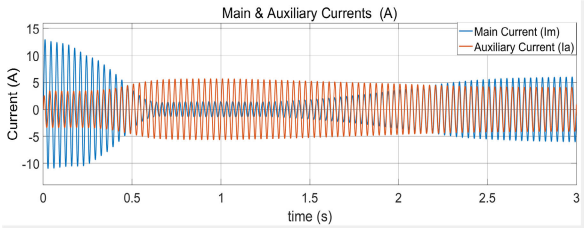

(b) Main and auxiliary currents at $f = 30$ Hz under the constant V/f control method.

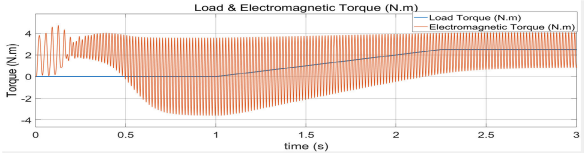

(c) Load and electromagnetic torque at $f = 30$ Hz under the constant V/f control method.

FIGURE 13. Simulation-based results of SPIM operation under the constant V/f control method at $f = 30$ Hz.

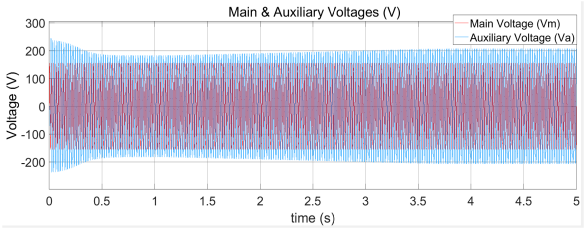

(a) Main and auxiliary voltages at $f = 60$ Hz under the proposed optimal control strategy.

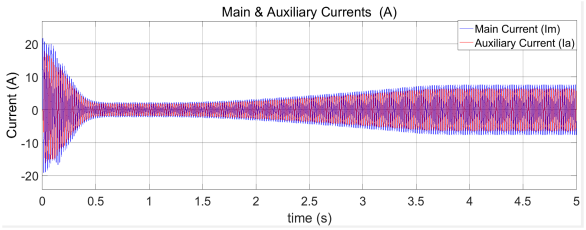

(b) Main and auxiliary currents at $f = 60$ Hz under the proposed optimal control strategy.

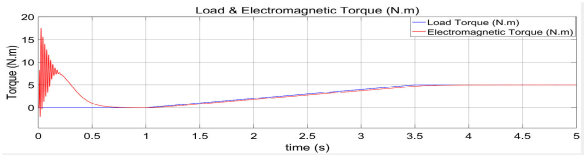

(c) Load and electromagnetic torque at $f = 60$ Hz under the proposed optimal control strategy.

FIGURE 14. Simulation-based results of SPIM operation under the proposed optimal control strategy at $f = 60$ Hz.

TABLE 2. SPIM Performance Comparison at Different Frequencies.

(a) SPIM performance comparison at 10Hz.

SPIM Performance	Constant V/f		Phase-Shift Algorithm	
τ_{load} (N.m)	0.5	1.0	0.5	1.0
Slip %	25	100	12	33.33
P_{out} (Watts)	11.7	0	13.9	21
Power Gain			19%	∞

(b) SPIM performance comparison at 30Hz.

SPIM Performance	Constant V/f		Phase-Shift Algorithm	
τ_{load} (N.m)	2.5	2.9	2.5	2.9
Slip %	28.4	47.8	21.1	24.4
P_{out} (Watts)	168	145	185	215
Power Gain			10.22%	48.2%

(c) SPIM performance comparison at 60Hz.

SPIM Performance	Constant V/f		Phase-Shift Algorithm	
τ_{load} (N.m)	3.0	5.0	3.0	5.0
Slip %	19.3	100	11.5	22.3
P_{out} (Watts)	458	0	500	732
Power Gain			9.1%	∞

In this implementation, the magnitudes of $\boldsymbol{V_a}$ and $\boldsymbol{V_m}$ are controlled by the phase-shift algorithm by adjusting the modulation index as discussed in section 4. This eliminates the need for DC-DC converter, thus making the proposed control strategy affordable and attractive to the local industry.

To evaluate the efficiency improvement of the proposed control strategy during operating conditions, and to observe the effects of loading process at varying frequencies, a linear load is activated at $t = 1s$. To evaluate the performance improvement during soft-starting at low frequencies, a linear load is activated at $t = 0s$ to mimic the real-world conditions.

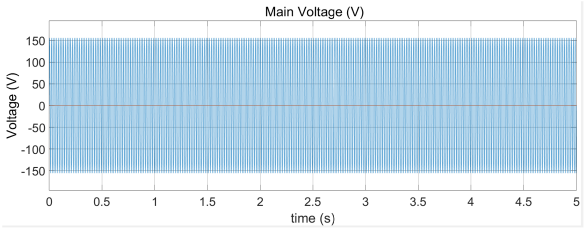

(a) Main voltage at $f = 60$ Hz under the constant V/f control method.

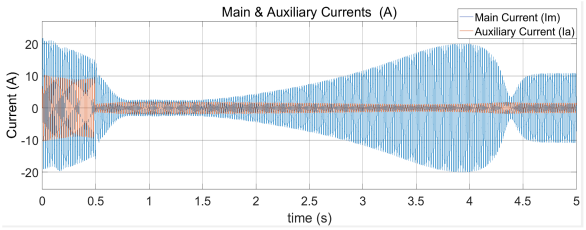

(b) Main and auxiliary currents at $f = 60$ Hz under the constant V/f control method.

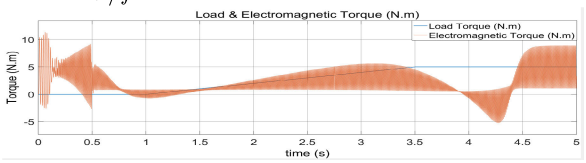

(c) Load and electromagnetic torque at $f = 60$ Hz under the constant V/f control method.

FIGURE 15. Simulation-based results of SPIM operation under the constant V/f control method at $f = 60$ Hz.

VII. RESULTS AND DISCUSSION

To validate the efficiency improvement offered by the proposed control technique, the performance of SPIM under the phase-shift algorithm is evaluated at low, medium and high operating frequencies with non-rated starting and operating conditions. To prove the superiority of the proposed control strategy, the simulation-based results of the phase-shift algorithm are compared with the corresponding results of constant V/f method.

For medium non-rated operating frequency of 30Hz, Fig. 12a shows that ϕ_v and V_a are updated continuously according to (22) and (26) for the formation of circular magnetic field inside SPIM. In Fig. 12c, it can be observed that the torque pulsations have been eliminated under the proposed strategy and SPIM meets/counters the required load-torque smoothly. The elimination of torque pulsations indicates the formation of circular magnetic field, and a balanced and symmetrical operation of SPIM. Same results are observed for the proposed control strategy at $f = 60$ Hz and $f = 10$ Hz in Figs 14c and 16c respectively.

Fig. 12b shows that SPIM under the phase-shift algorithm draws significantly less I_m both during the unloaded and loaded conditions for a particular operating frequency. For SPIM operating under the proposed strategy, I_m increases

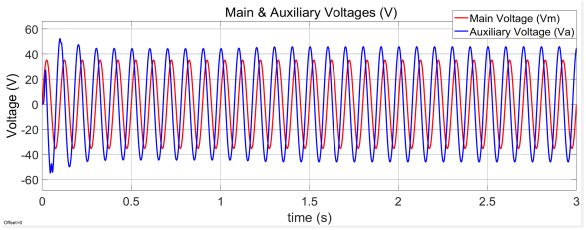

(a) Main and auxiliary voltages at $f = 10$ Hz under the proposed optimal control strategy.

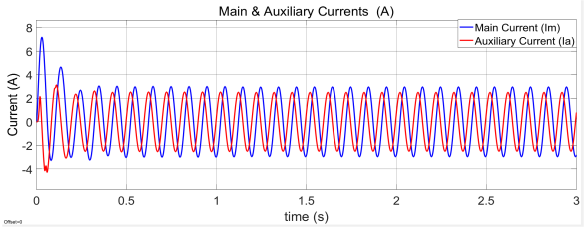

(b) Main and auxiliary currents at $f = 10$ Hz under the proposed optimal control strategy.

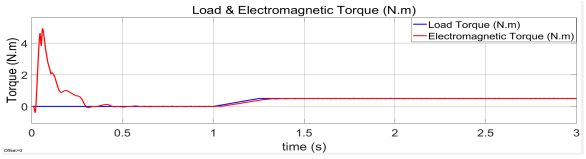

(c) Load and electromagnetic torque at $f = 10$ Hz under the proposed optimal control strategy.

FIGURE 16. Simulation-based results of SPIM operation under the proposed optimal control strategy at $f = 10$ Hz.

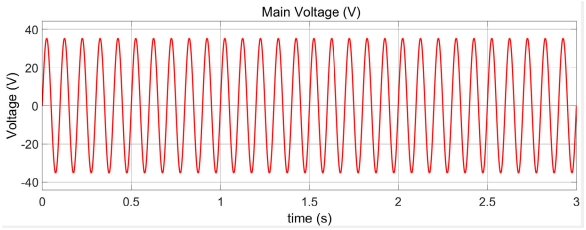

(a) Main voltage at $f = 10$ Hz under the constant V/f control method.

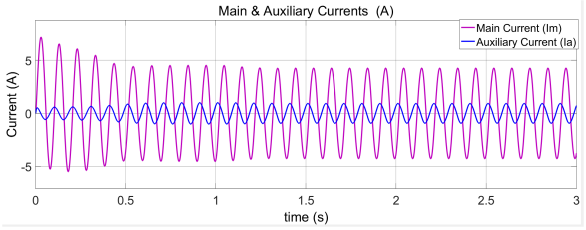

(b) Main and auxiliary currents at $f = 10$ Hz under the constant V/f control method.

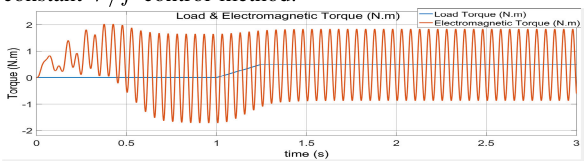

(c) Load and electromagnetic torque at $f = 10$ Hz under the constant V/f control method.

FIGURE 17. Simulation-based results of SPIM operation under the constant V/f control method at $f = 10$ Hz.

smoothly with no torque oscillations as it transitions to loaded state at $t = 1s$, which reflects the dynamic update of ϕ_v and V_a during the transition to maintain a symmetric SPIM operation.

However, according to Fig. 13b, 15b and 17b, for SPIM operating under the constant V/f method, I_m increases steeply as the SPIM moves farther away from the rated operating point when load is activated at $t = 1s$. The resulting increase in magnetic field distortion and torque pulsations with deviation in operating point seriously degrades the efficiency of SPIM. This inefficient operation of SPIM under the constant V/f method is reflected through a steep increase in I_m simultaneously with a drastic increase in slip.

The effect of excursion of operating point from rated-conditions on SPIM efficiency is significant in Fig. 13b. At 30 Hz, due to reduced frequency and significant load-torque of 2.5 N.m, SPIM under the constant V/f method operates significantly far from its rated operating point and draws a huge current I_m of 6.5 A when loaded. Therefore, a significant reduction in I_m is observed in Fig. 12b as its magnitude reduces to 3.8 A for SPIM operation under the proposed algorithm.

For SPIM operation at 30Hz, the fact that SPIM efficiency degrades as its operating point moves away from the rated conditions is also confirmed by Table 2b. This tables shows that a power gain of 10.22% is obtained at τ_{load} =2.5 N.m, and an increased power gain of 48.2% is obtained at τ_{load} = 2.9 N.m under the proposed control strategy. In Table 2, similar effect is observed at other frequencies. Thus, as SPIM moves away from the rated operating point through a change in frequency or load-condition, the efficiency gain offered by the phase-shift algorithm increases. Therefore, this confirms the fact that the proposed control strategy perfectly complements the variable speed operation of SPIM at low-frequencies and varying load-conditions.

At 60 Hz, Fig 15c shows that SPIM under constant V/f method is unable to meet non-rated load load torque of 5 N.m. However, from Fig. 14c, it is clear that SPIM under the phase-shift algorithm develops the required torque of 5 N.m with no pulsations. Therefore, it confirms the analysis that for a particular frequency, as the magnetic field becomes circular, SPIM develops increased torque at a given slip, which means less input power and improved efficiency are observed. This fact is confirmed by Table 2 which indicates that SPIM under the proposed control technique develops/meets the required load-torque with comparatively reduced slip. This reduced slip operation leads to less I_m being drawn and thus more efficient operation at a particular load is possible for a given frequency. In Table 2, similar effect can be observed at other frequencies as well. This confirms the analysis that the proposed control increases the efficiency of SPIM by significantly reducing current per torque.

Even at 10 Hz, the torque pulsations are eliminated under the phase-shift algorithm as shown in Fig. 16c, which reflects the dynamic and timely update of ϕ_v and V_a.

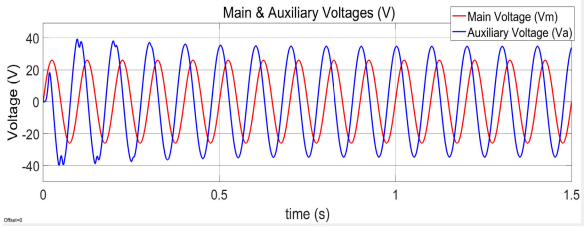

(a) Main and auxiliary voltages for soft-starting at $f = 10$ Hz under the proposed soft-starting strategy.

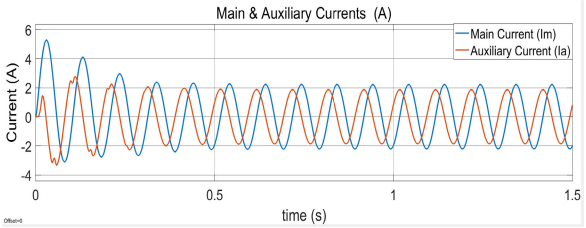

(b) Main and auxiliary currents for soft-starting at $f = 10$ Hz under the proposed soft-starting strategy.

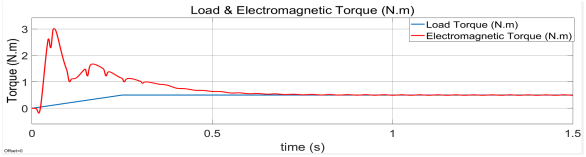

(c) Load and electromagnetic torque for soft-starting at $f = 10$ Hz under the proposed soft-starting strategy.

FIGURE 18. Simulation-based results of SPIM soft-starting at $f = 10$ Hz under the proposed soft-starting strategy.

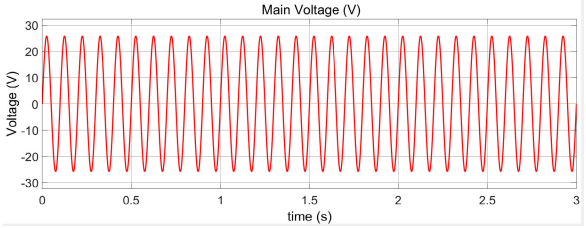

(a) Main voltage for soft-starting at $f = 10$ Hz under the constant V/f method.

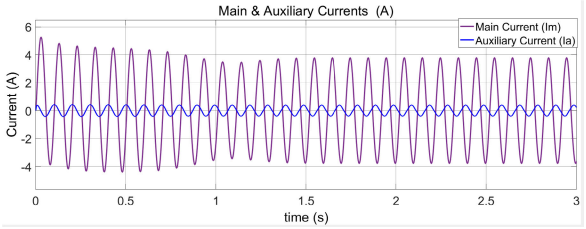

(b) Main and auxiliary currents for soft-starting at $f = 10$ Hz under the constant V/f method.

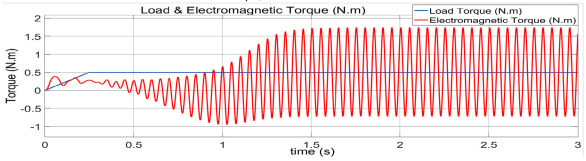

(c) Load and electromagnetic torque for soft-starting at $f = 10$ Hz under the constant V/f method.

FIGURE 19. Simulation-based results of SPIM soft-starting at $f = 10$ Hz under the constant V/f control method.

Fig. 18b shows that for soft-starting under the proposed optimal starting control, I_m settles to $2A$ within $t = 0.3s$. However, for SPIM starting under conventional techniques, Fig. 19b shows that I_m stays above $4A$ till $t = 0.7s$ and then finally starts to settle down to $4A$. This confirms the analysis that the proposed control improves the starting efficiency of SPIM.

Comparing Fig. 16c with Fig. 17c, it can be seen that SPIM operation under the proposed optimal control significantly reduces the starting torque oscillations even at low frequencies. The elimination of torque pulsations, in turn, reflects the formation of circular magnetic fields and balanced SPIM operation enabled by the continuous update of optimal V_a and ϕ_v. This balanced and symmetric operation increases the starting torque and SPIM is able to overcome small load present at the starting conditions in industrial applications. This analysis is confirmed by Fig. 18c, which shows that SPIM can successfully soft-start at 10 Hz under linear starting load. However, according to Fig. 19c, the SPIM operating under constant V/f fails to start due to the distortion of magnetic field and the resulting degradation of starting torque at low-frequencies. The soft-starting of SPIM at low-frequencies, in turn, causes a reduction in inrush current, which is evident in Fig. 18b. Comparing Fig. 18b with Fig. 15b, it can be seen that the soft-starting of SPIM under the proposed technique results in an inrush current reduction of more than 84%. Soft-starting at even lower frequencies can further reduce the inrush current.

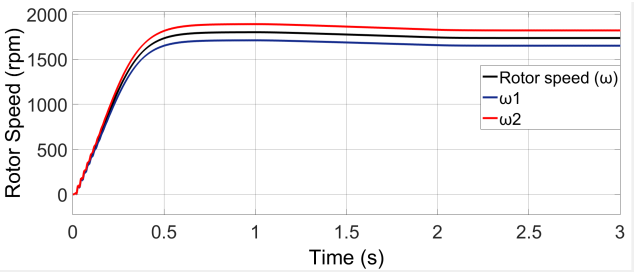

FIGURE 20. The system's response as a result of $+/-$ 5% error introduced in ω.

The performance of the phase-shift algorithm is studied under $+/-$ 5% feedback error conditions as shown in Fig. 20. Even a significant error introduced in the feedback rotor-speed signal results in negligible torque pulsations as shown in Fig 21. In Fig 21, τ represents the torque developed when the system receives an accurate rotor-speed feedback, $\tau_{\omega 1}$ and $\tau_{\omega 2}$ represent the torque developed when the rotor-speed feedback is varied by -5% and $+5\%$ of its accurate value respectively. This shows that the phase-shift algorithm is robust and resistant to errors in speed-sensor output. Moreover, as shown in Fig. 20, the system maintains its stability throughout even when significant errors are purposefully introduced in the feedback loop.

In most of the industrial applications, the load torque on SPIM remains constant. Under such predictable conditions, the trajectories of optimal ϕ_v and V_a can be saved in a

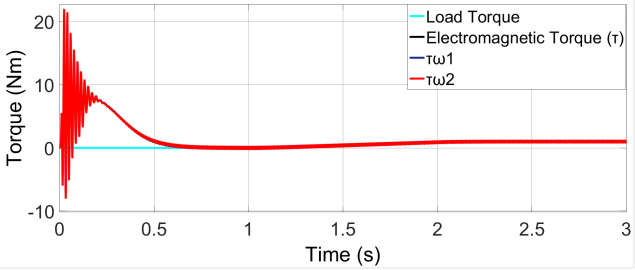

FIGURE 21. Load torque τ_{load} and developed torques under different feedback error conditions.

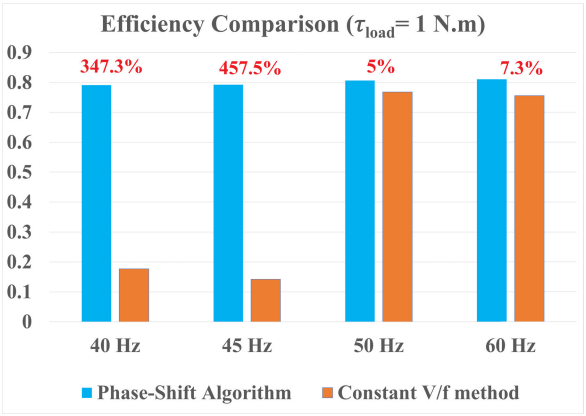

(a) Efficiency comparison at load-torque τ_{load} = 1 N.m.

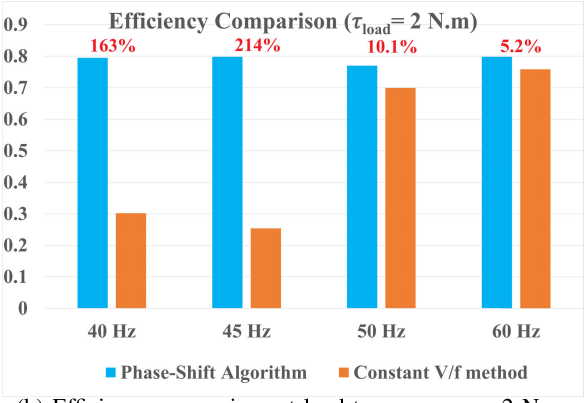

(b) Efficiency comparison at load-torque τ_{load} = 2 N.m.

FIGURE 22. Efficiency improvement offered by the phase-shift algorithm under different non-rated operating and load conditions.

look up table. As the phase-shift algorithm is resistant to small disturbances (errors) in the system and maintains a stable system operation, these saved trajectories in the form of look up tables can then be used to operate the SPIM in the proposed improved efficiency mode. Therefore, in most industrial applications, phase-shift algorithm eliminates the need of the feedback loop and a look up table based technique can be implemented if the system disturbances remain within the satisfactory error margins.

Using the test-setup as shown in Fig. 11, the efficiency of SPIM under the phase-shift algorithm is compared with the constant V/f method. Fig. 22 shows the efficiency improvement offered by the phase-shift algorithm under different non-rated operating and load conditions. The percent increase in efficiency is indicated in red in Fig. 22. It is verified that the phase-shift algorithm is a powerful algorithm which can offer efficiency improvement of more than 400%.

VIII. CONCLUSION

In this article, it is demonstrated that conventional techniques for speed control of SPIMs are inefficient because they cause the formation of elliptical magnetic fields inside them at non-rated starting and operating conditions. After a detailed analysis of SPIM energy-efficiency, a novel sensor-less control strategy was devised to improve the performance at non-rated conditions by enabling the symmetrical and balanced operation of SPIM. Formation of circular magnetic field inside SPIMs over the entire speed range is achieved by dynamically and optimally controlling the auxiliary voltage and phase-difference between the windings voltages simultaneously with constant V/f control using the developed phase-shift algorithm. Simulation-based evaluation of the optimal control strategy demonstrates an improvement of more than 400% in energy-efficiency as compared to maximum 18% reported in case of conventional SPIM energy-efficiency optimization techniques. The developed control algorithm also enables the soft-starting of SPIM with substantial starting torque at low-frequencies, resulting in a significant reduction in inrush current. Simulation-based results of the proposed sensor-less optimal control strategy confirm an inrush current reduction of more than 84%. This efficient soft-starting results in further energy-savings.

ACKNOWLEDGEMENT

This work was supported by the Kuwait Foundation for the Advancement of Sciences (KFAS), under Project PR18-18EO-01.

REFERENCES

[1] J. C. Gomez, C. Reineri, G. Campetelli, and M. M. Morcos, "A study of voltage sags generated by induction motor starting," *Electr. Power Compon. Syst.*, vol. 32, no. 6, pp. 645–653, Jun. 2004.

[2] X. Wang, J. Yong, W. Xu, and W. Freitas, "Practical power quality charts for motor starting assessment," *IEEE Trans. Power Del.*, vol. 26, no. 2, pp. 799–808, Apr. 2011.

[3] Z. B. Duranay and H. Guldemir, "Selective harmonic eliminated V/f speed control of single-phase induction motor," *IET Power Electron.*, vol. 11, no. 3, pp. 477–483, Mar. 2018.

[4] A. Sampathkumar, "Speed control of single phase induction motor using V/f technique," *Middle-East J. Sci. Res.*, vol. 16, no. 12, pp. 1807–1812, 2013.

[5] E. R. Collins, "Torque and slip behavior of single-phase induction motors driven from variable-frequency supplies," *IEEE Trans. Ind. Appl.*, vol. 28, no. 3, pp. 710–715, May/Jun. 1992.

[6] S. Chen and S.-N. Yeh, "Optimal efficiency analysis of induction motors fed by variable-voltage and variable-frequency source," *IEEE Trans. Energy Convers.*, vol. 7, no. 3, pp. 537–543, Sep. 1992.

[7] S. Vaez-Zadeh and A. Payman, "Design and analysis of sensorless torque optimization for single phase induction motors," *Energy Conv. Mangmt.*, vol. 47, pp. 1464–1477, Jul. 2006.

[8] D. Y. Um and G. S. Park, "Determination scheme of stator parameters for making rotating fields circular in a single-phase induction motor," *IEEE Trans. Magn.*, vol. 56, no. 1, pp. 1–5, Jan. 2020.

[9] X. Wang, H. Zhong, Y. Yang, and X. Mu, "Study of a novel energy efficient single-phase induction motor with three series-connected windings and two capacitors," *IEEE Trans. Energy Convers.*, vol. 25, no. 2, pp. 433–440, Jun. 2010.
[10] R. Mera and R. Campeanu, "Optimal performance of capacitor-run single phase induction motor," in *Proc. 13th Int. Conf. Optim. Electr. Electron. Equip. (OPTIM)*, May 2012, pp. 718–723.
[11] M. Chomat and T. A. Lipo, "Adjustable-speed single-phase IM drive with reduced number of switches," *IEEE Trans. Ind. Appl.*, vol. 39, no. 3, pp. 819–825, May 2003.
[12] S. Vaez-Zadeh and H. Langari, "High average-low pulsating torque operation of single phase induction motors," in *Proc. 35th Conf. Rec. IEEE Ind. Appl. Conf. IAS Annu. Meeting World Conf. Ind. Appl. Electr. Energy*, Oct. 2000, pp. 1513–1518.
[13] H. Langari and S. Vaez-Zadeh, "DSP based optimal torque control of single-phase induction motors," in *Proc. IEEE 32nd Annu. Power Electron. Spec. Conf.*, Jun. 2001, pp. 850–855.
[14] C. Mademlis, T. Theodoulidis, and I. Kioskeridis, "Optimization of single-phase induction motors—Part II: Magnetic and torque performance under optimal control," *IEEE Trans. Energy Convers.*, vol. 20, no. 1, pp. 196–203, Mar. 2005.
[15] W. S. Abu-Elhaija and A. Muetze, "Effect of the variation of the rotor impedance with slip on the performance of single-phase excited three-phase induction motors," *IEEE Trans. Energy Convers.*, vol. 25, no. 4, pp. 1010–1020, Dec. 2010.
[16] K. Sundareswaran, "An improved energy-saving scheme for capacitor-run induction motor," *IEEE Trans. Ind. Electron.*, vol. 48, no. 1, pp. 238–240, Feb. 2001.
[17] C. Mademlis, I. Kioskeridis, and T. Theodoulidis, "Optimization of single-phase induction motors—Part I: Maximum energy efficiency control," *IEEE Trans. Energy Conv.*, vol. 20, no. 1, pp. 187–195, Mar. 2005.
[18] B. Zahedi and S. Vaez-Zadeh, "Efficiency optimization control of single-phase induction motor drives," *IEEE Trans. Power Electron.*, vol. 24, no. 4, pp. 1062–1070, Apr. 2009.
[19] N. Abdel-Rahim and A. Shaltout, "Operation of single-phase induction motor as two-phase motor," in *Proc. IEEE 28th Annu. Conf. Ind. Electron. Society. (IECON)*, vol. 2, Nov. 2002, pp. 967–972.
[20] E. Muljadi, Y. Zhao, T.-H. Liu, and T. A. Lipo, "Adjustable AC capacitor for a single-phase induction motor," *IEEE Trans. Ind. Appl.*, vol. 29, no. 3, pp. 479–485, May/Jun. 1993.
[21] M. B. de Rossiter Correa, C. B. Jacobina, E. R. C. da Silva, and A. M. N. Lima, "Vector control strategies for single-phase induction motor drive systems," *IEEE Trans. Ind. Electron.*, vol. 51, no. 5, pp. 1073–1080, Oct. 2004.
[22] P. C. Sen, *Principles of Electric Machines & Power Electronics*. Hoboken, NJ, USA: Wiley, 2007.
[23] M. Lakka, E. Koutroulis, and A. Dollas, "Development of an FPGA-based SPWM generator for high switching frequency DC/AC inverters," *IEEE Trans. Power Electron.*, vol. 29, no. 1, pp. 356–365, Jan. 2014.
[24] S. Z. M. Noor, M. K. Hamzah, N. F. A. Rahman, A. F. Hapani, and Z. Idris, "XILINX FPGA design for sinusoidal pulse width modulation (SPWM) control of single-phase matrix converter," in *Proc. IEEE Symp. Ind. Electr. Appl.*, Sep. 2011, pp. 714–719.
[25] R. K. Pongiannan, P. Selvabharathi, and N. Yadaiah, "FPGA based three phase sinusoidal PWM VVVF controller," in *Proc. 1st Int. Conf. Electr. Energy Syst.*, Jan. 2011, pp. 34–39.
[26] M. A. Rongi, A. Saparon, and M. K. Hamzah, "Sinusoidal pulse width modulation using CORDIC algorithm for single phase matrix converter," in *Proc. 5th IEEE Conf. Ind. Electron. Appl.*, Jun. 2010, pp. 1088–1093.
[27] K.-T. Chen, K. Fan, X. Han, and T. Baba, "A CORDIC algorithm with improved rotation strategy for embedded applications," *J. Ind. Intell. Inf.*, vol. 3, no. 4, pp. 274–279, 2015.

MUHAMMAD NOMAN ALMANI received the B.Sc. degree in electrical engineering from the University of Engineering and Technology Lahore, in 2017. He is currently pursuing the prospective Ph.D. degree with the Electrical and Computer Engineering Department, University of Florida, Gainesville. As a Research Assistant, he has since worked on various research grants in the areas of electric machines, control theory, and machine learning. His research interests include the intersection of control theory and machine learning particularly reinforcement learning.

GHULAM AMJAD HUSSAIN (Senior Member, IEEE) received the bachelor's degree in electrical engineering from the University of Engineering and Technology, Lahore, Pakistan, in 2007, and the master's and Ph.D. degrees from the School of Electrical Engineering, Aalto University, Finland, in 2012 and 2016, respectively. He was a Senior R&D Engineer-Power Systems Technologies with the EATON European Innovation Centre (EEIC), Prague, Czech Republic. He is currently an Assistant Professor with the American University of Kuwait, Kuwait, where he is involved in teaching and research. He has authored or coauthored more than 40 articles in international journals and conferences and has one patent. His research interests include high voltage engineering, power system protection, control in modern smart grids, and power system analysis.

ASHRAF A. ZAHER (Senior Member, IEEE) received the B.E. degree in electronics and communication engineering and the M.E. degree in automatic control engineering from Mansoura University, Egypt, in 1988 and 1994, respectively, the first Ph.D. degree in systems engineering from Oakland University, MI, USA, in 2001, and the second Ph.D. degree in control engineering from Oakland/Mansoura Universities (joint supervision), in 2004. He is currently a Professor with the American University of Kuwait. He participated in many projects, received many grants, and published several technical reports in the field of virtual engineering applications in the automotive industry. He has plenty of publications in both international journals and conferences, and serves as a reviewer for various journals. His research interests include virtual engineering, nonlinear dynamics, hybrid signal processing, engineering physics, and chaos. He is a Senior Member of AACC and AIP.